# Land Cover Changes of the Qilian Mountain National Park in Northwest China Based on Phenological Features and Sample Migration from 1990 to 2020

**Yanyun Nian *** , **Zeyu He, Wenhui Zhang** and **Long Chen**

Key Laboratory of Western China's Environmental Systems (Ministry of Education), College of Earth and Environmental Sciences, Lanzhou University, Lanzhou 730000, China
* Correspondence: yynian@lzu.edu.cn

**Abstract:** The spatial and temporal variation analysis of land cover classification is important for studying the distribution and transformation of regional land cover changes. The Qilian Mountain National Park (QMNP), an important ecological barrier in northwestern China, has lacked land cover products for long time series. The Landsat images available on the Google Earth Engine (GEE) make it possible to analyze the land cover changes over the past three decades. The purpose of this study was to generate a long time series of datasets of land cover classification based on the method of sample migration in the QMNP in Northwest China. The Landsat 5, 7, and 8 images and field sample data were combined with multiple image features and the random forest algorithm to complete the land cover classification of the QMNP from 1990 to 2020. The results indicate that (1) the method of Jeffries–Matusita (J-M) distance can reduce image feature redundancy and show that elevation and phenological features have good differentiability among land cover types that were easy to mix with feature classes; (2) the spatial distribution of land cover every 10 years between 1990 and 2020 was consistent in the QMNP, and there were obvious differences in land cover from the east to the west part of the QMNP, with a large area of vegetation distribution in Sunan county in the central part and Tianzhu county in the east part of the QMNP; (3) over the past 30 years, forests and grasslands decreased by 62.2 km$^2$ and 794.7 km$^2$, respectively, while shrubs increased by 442.9 km$^2$ in the QMNP. The conversion of bare land to grassland and the interconversion between different vegetation types were the main patterns of land cover changes, and the land cover changes were mainly concentrated in pastoral areas, meaning that human activity was the main factor of land cover changes; and (4) when the samples of 2020 were migrated to 2010, 2000, and 1990, the overall classification accuracies were 89.7%, 88.0%, 86.0%, and 83.9%, respectively. The results show that the vegetation conservation process in the QMNP was closely related to human activities.

**Keywords:** Landsat; sample migration; Jeffries–Matusita distance; machine learning

## 1. Introduction

Land cover is an important factor for assessing ecological change in alpine mountains in Northwest China [1]. Land cover, especially vegetation, in most areas of Northwest China is ecologically diverse and fragile [2]. The Qilian Mountain National Park (QMNP) is one of the first pilots of the national park system in China established since 2017 and is an important ecological safety barrier in the alpine-type mountains of Northwest China [3].

Over the past several decades, long-term ecological services have been seriously affected. Ecosystems in nature and their biodiversity are endangered by human-induced causes [4]. The ecological environment in the Qilian Mountains has been damaged to varying degrees by overgrazing, unauthorized construction of hydropower stations, unregulated operation of tourism facilities, and other human activities [5]. Land cover and land management influence soil and water conservation, environmental protection, etc.,

for example, via its contribution to river changes [6]. Therefore, making a long time series of land cover data products and analyzing the spatiotemporal changes in vegetation are essential to quickly capture the characteristics of vegetation change in the QMNP. There is still a lack of sufficiently detailed classification and long time series of land cover data to reflect the typical changes in vegetation, which results in a poor understanding of the long-term impacts of vegetation in the QMNP [7]. With the development of sensors and cloud computing technology, the acquisition and analysis of land cover data have developed rapidly. Currently, object-based and pixel-based classification methods are widely used for land cover classification. Yu et al. [8] presented an object-based backdating approach that increases the efficiency of land use and land cover classification. Lu et al. [9] proposed an object-based data blending model based on Landsat and MODIS to detect land cover changes. Aguirre-Gutierrez et al. [10] combined object-based and pixel-based methods and found the combined classification method improved classification accuracy and land cover change detection. Tehrany et al. [11] obtained the results of land cover classification in Selangor using object-based and pixel-based methods; the results showed that the object-based method performed better. The object-based method needs to determine the optimal segmentation scale and requires high spatial resolution of remote sensing images, so it is subject to some limitations in land cover data analysis [12]. The pixel-based method is simple, but the accuracy of the result depends more on the classification system and the classification algorithm.

Cloud computing platforms are efficient ways of accessing and analyzing data on very powerful servers. Several cloud computing platforms have been developed to date. For example, the Google Earth Engine (GEE) provides researchers with new classification ideas due to its powerful data storage function and computing power so that they can pay more attention to the optimization of the classification processes of land cover from remote sensing images [13]. It is difficult to accurately classify vegetation only by vegetation indices and other auxiliary data, while phenological features are good supplementary data to distinguish different vegetation types. The extraction of phenological features from time series normalized difference vegetation index (NDVI) curves for more detailed land cover classification has received widespread attention from researchers. Reed et al. [14] were the first to propose the use of phenological features. Nguyen et al. [15] extracted parameters such as coefficients based on the time series enhanced vegetation index (EVI) curves of crops from Landsat data, which they used as a phenological feature in land cover classification. Zeng et al. [16] reviewed the existing methods for weather detection in detail and showed that the extraction of thresholds based on vegetation index time series curves is the simplest and most effective method in vegetation phenological extraction that is widely used for phenological metric extraction. In addition, the acquisition of samples from multiple years in long time series land cover studies has been a focus of researchers. Huang et al. [17] migrated the training samples of 2010, 2005, 2000, 1995, and 1990 based on the sample set of 2015 and all available Landsat 5 data on GEE by measuring the spectral similarity and spectral distance between the reference and target spectra. Naboureh et al. [18] migrated the samples of 2020 based on the spectral distance to obtain the sample set of 1987–2019 and extracted the farming area of the Urmia Lake basin with good results. Ghorbanian et al. [19] obtained the land cover products for the whole of Iran in 2019 based on the classification results of 2017 and the sample migration method of spectral distance with an accuracy greater than 90%. Sample migration based on spectral distance has become an important technical tool for multiyear land cover classification. It makes up for the shortage of training samples and greatly improves classification efficiency. Huang et al. [20] developed a new sample migration method combined with other strategies to effectively support long time series global land cover mapping. Liu et al. [21] combined sample migration, machine learning, and other methods to generate a 36-year-long, 30 m resolution global land cover map dataset. Zhong et al. [22] used a sample migration method to obtain data for the the earlier years from the 2011–2015 Landsat data and produced a long time series land cover dataset based on a machine learning method.

The Landsat dataset, field data, the GEE platform with machine learning algorithms, phenological features, and the sample migration method allowed us to obtain previous sample data and land cover classification results for QMNP. Therefore, to solve the problem of a lack of long time series land cover change analysis of the QMNP, this study uses phenological features and sample migration methods to analyze land cover changes. The main objectives of this paper are (1) to develop a sample selection method for land cover classification in long time series, (2) to explore the optimal combination of features based on Landsat data for complex mountainous terrain, and (3) to analyze the land cover changes based on the QMNP classification results to reveal ecological changes and better protect the ecological barrier.

## 2. Materials and Methods

A classification process based entirely on the GEE applied to QMNP is proposed in this study. Figure 1 describes the main procedures of this study. The time series images of the target years were mosaicked and synthesized using the available Landsat images in the GEE. Then, sample migration was performed to obtain sample sets of the target year, optimize the feature set, and finally, use a random forest algorithm to complete land cover classification for four periods. The method used in this study is summarized as follows:

i. Data processing, including image declouding and mosaicking, as well as sample point selection for 2020;

ii. Sample migration, which was achieved by measurements of spectral angles;

iii. Feature extraction, which mainly includes time series curve reconstruction and phenology parameter extraction;

iv. Classification using the random forest algorithm, optimization of algorithm parameters, and accuracy assessment;

v. Land cover change analysis through transfer matrix and land mapping.
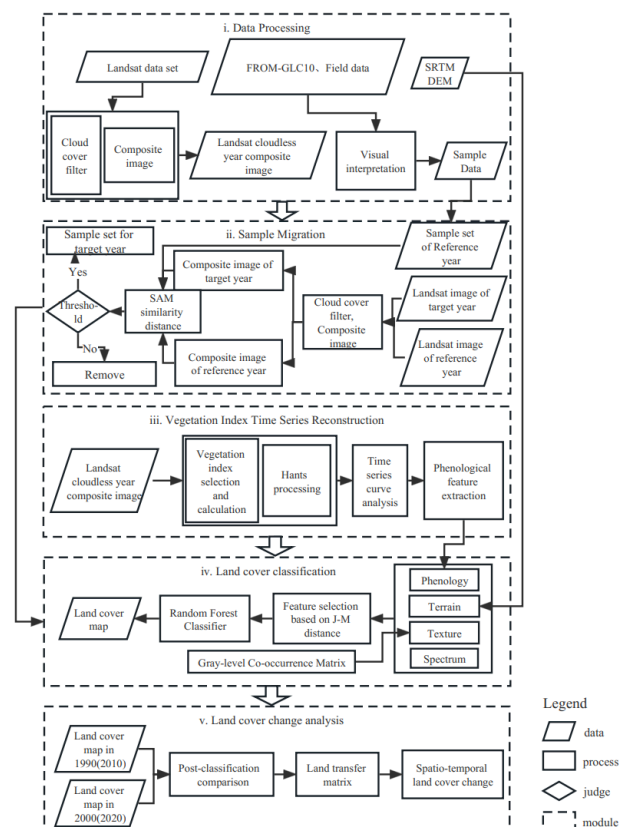
**Figure 1.** Workflow of sample migration, phenological feature extraction, and land cover classification on the GEE.

*2.1. Study Area*

The study area is located in the Qilian Mountains (95°~103°E, 36°~40°N, Figure 2) at the junction of the Gansu and Qinghai Provinces [23]. The QMNP climate is humid in the summer and dry and cold in the winter, with shorter summers and longer winters [24]. The large east–west span of the region leads to obvious climatic differences, with the west being cold and dry, the central area being alpine and semiarid, and the east being alpine and semihumid [25]. Precipitation decreases from the east to the west and is mainly concentrated from May to September. The main vegetation types in the QMNP are forest, shrub, and grassland. The forests are mainly natural forests supplemented by planted forests, and the types include temperate evergreen coniferous forests, temperate deciduous broadleaf forests, mixed coniferous forests, and cold-temperate coniferous forests [26]. Among them, *Picea crassifolia* and *Juniperus przewalskii* are the dominant species, accounting for 88.9% and 95.06% of the area and storage volume, respectively [25].
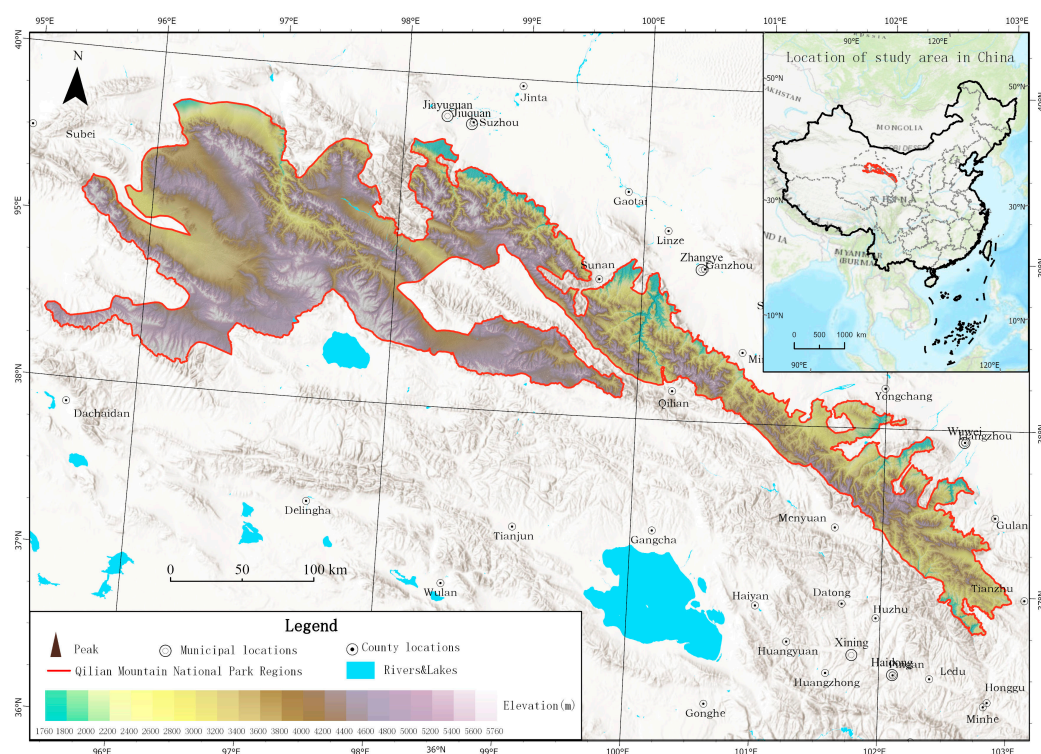
**Figure 2.** Location of the Qilian Mountain National Park.

*2.2. Classification Scheme*

The classification system of this study was based on the situation that the QMNP is mainly dominated by vegetation cover, with *Picea crassifolia* and *Juniperus przewalskii* as the dominant species, and with reference to two classification systems: the International Geosphere-Biosphere Programme (IGBP) and Global Land Cover 2000 (GLC2000). Twelve categories were ultimately determined. Evergreen conifer forests in the IGBP and GLC2000 classifications were subdivided into *Picea crassifolia* and *Juniperus przewalskii*; evergreen shrubs and deciduous shrubs in GLC2000 were retained; and typical feature types such as snow and ice, water bodies, and arable land were retained. The category names and interpretation marks are shown in Table 1.

**Table 1.** Interpretation signs of land cover.

| First Class | Second Class | Third Class | Abbreviation | Description | Elevation Range |
|---|---|---|---|---|---|
| Forest | Evergreen Needleleaf Forest | *Picea crassifolia* | PC | Needle-leaved, evergreen; >85% of the forest is composed of *Picea crassifolia*, including plantations; H = 3–30 m | 2500–3600 m |
| | Evergreen Needleleaf Forest | *Juniperus przewalskii* | JP | Needle-leaved, evergreen; >85% of the forest is composed of *Juniperus przewalskii*, including plantations | 2700–4000 m |
| | Broadleaf Forest | Broadleaf Forest | BF | Flattened, broader, deciduous leaves; >85% broadleaf trees in the forest, including plantations | 1900–2700 m |
| | Mixed Forest | Mixed Forest | MF | The respective proportions of coniferous and broad-leaved forests ranged from 25% to 75% and were above 3 m in height, including planted forests | 2500–2900 m |
| Shrubland | Evergreen Shrub | Evergreen Shrub | ES | Plant communities dominated by coniferous shrubs less than two meters in height | 3000–3700 m |
| | Deciduous Shrub | Deciduous Shrub | DS | Plant communities dominated by deciduous shrubs less than two meters in height | 1900–3700 m |
| Grassland | Grassland | Grassland | G | Plant community dominated by annual or perennial herbaceous vegetation, including land in a managed state such as human grazing and harvesting | 1700–3000 m & 3500–4200 m |
| Agricultural Lands | Cropland | Cropland | C | Refers to land on which crops are grown | Below 2500 m |
| Impervious Surface | Impervious Surface | Impervious Surface | IS | Cities, towns, villages, and other settlements and roads, as well as artificial hard surfaces | Below 2500 m |
| Water | Water | Water | W | Including natural and artificially constructed relatively stationary water surfaces | - |
| Snow and Ice | Snow and Ice | Snow and Ice | SI | Land whose surface is covered by ice and snow year-round | Above 4600 m |
| Desert and Low-vegetated Lands | Desert and Bare soil | Bare Land | BL | Land with surface covered by soil and loose structure | 4200–4600 m |

### 2.3. Data

2.3.1. Remote Sensing Dataset

Landsat images and other ancillary datasets were used to complete the land cover classification for each decade from 1990 to 2020. The Landsat data include Landsat 8 surface reflectance data for 2019 and 2020; Landsat 5 surface reflectance data for 1989, 1990, 2009, and 2010; and Landsat 7 surface emissivity data for 1999 and 2000, as shown in Table 2. These data were atmospherically corrected using the Landsat Ecosystem Disturbance Adaptive Processing System (LEDAPS) cloud algorithm [27] to produce a cloud, shadow, water, and snow mask using the C function of the Mask algorithm, as well as a per-pixel saturation mask [28]. Other ancillary data included Shuttle Radar Topography Mission

Digital Elevation Model (SRTM DEM) data and land cover data, i.e., Finer Resolution Observation and Monitoring of Global Land Cover (FROM-GLC10).

**Table 2.** Landsat image information.

| Year | Number of Images | Satellite | Date of Image Acquisition |
|------|------------------|-----------|---------------------------|
| 1990 | 509 | Landsat 5 TM | 1 January 1989–31 December 1990 |
| 2000 | 202 | Landsat 7 ETM+ | 1 January 1999–31 December 2000 |
| 2010 | 211 | Landsat 5 TM | 1 January 2009–31 December 2010 |
| 2020 | 666 | Landsat 8 OLI | 1 January 2019–31 December 2020 |

### 2.3.2. Field Data

The sample point data acquisition for this study in 2020 combined forest survey data, fieldwork data, and high-resolution Google Earth images to ensure accurate results of subsequent land cover classification. A total of 713 samples of field data included 482 sample data collected during the Second Tibetan Plateau Scientific Expedition and Research in 2018–2021 and 231 sample data from field work in 2022. A set of 745 sample images from forest resources survey data were used, and 2433 sample data were obtained from Google Earth data. The final distribution of sample points is shown in Figure 3. The field data were collected mainly by manual positioning and photographing. For some places inaccessible to humans, unmanned aerial vehicles (UAVs) were used to obtain field data. UAVs can facilitate the recording of high-quality remote sensing data [29]. The corresponding sample-level orthophotos and panoramic photos collected by UAVs are a reliable supplement to visual interpretation using Google Earth, especially solving the difficulty of discriminating *Picea crassifolia* and *Juniperus przewalskii* on Google Earth images, as shown in Table 3.
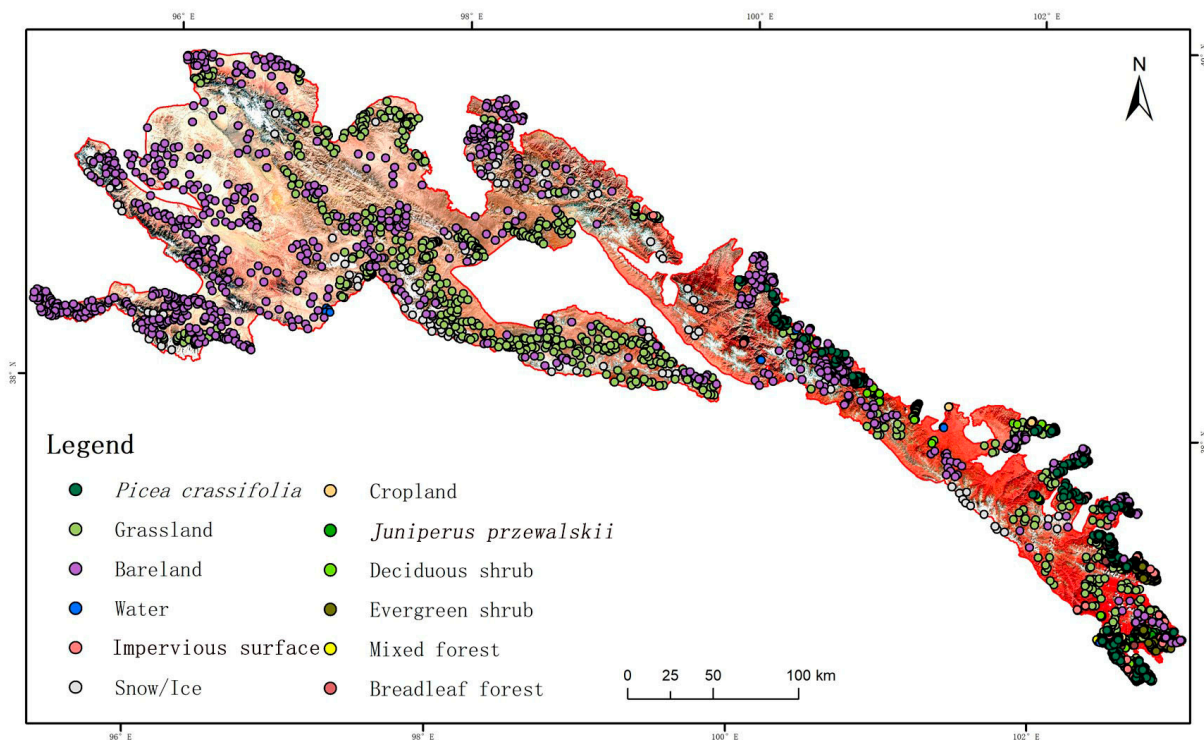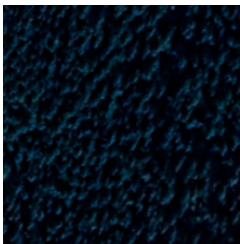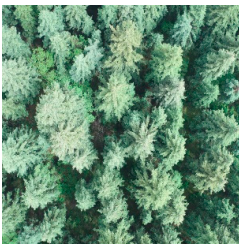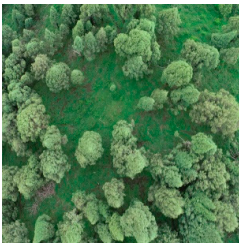
**Figure 3.** Spatial distribution of samples in 2020.

**Table 3.** Image comparison of Picea crassifolia and Juniperus przewalskii.

| Tree Species | Google Earth Image | Photo by Camera | UAV Orthophoto |
|---|---|---|---|
| *Picea crassifolia* | | | |
| *Juniperus przewalskii* | | | |

## 2.4. Methods

### 2.4.1. Feature Extraction

Various features were extracted in this study to improve the differentiability between land cover types. Spectral, textural, and topographic features based on Landsat data were extracted to make full use of the feature information of different land covers in remote sensing images. Four topographic features—slope, aspect, hill shade, and elevation—were generated using SRTM DEM data stored on the GEE to improve the accuracy of land cover classification in mountainous areas. Six texture features—angular second moment, variance, homogeneity, entropy, contrast, and correlation—were generated by the gray-level co-occurrence matrix (GLCM) method. The GLCM can describe the random and spatial statistical features of texture elements, fully consider the statistical features of the surrounding image elements, and greatly reduce the influence of sensors and weather on a single image element [30,31]. Additionally, three tasseled cap transformation features— brightness, greenness, and wetness—were calculated based on the remote sensing image bands [32]. Six spectral indices were calculated due to their good performance in differentiating vegetation types, the formulas of which are shown in Table 4: the normalized difference vegetation index (NDVI) [33], enhanced vegetation index (EVI) [34], soil-adjusted vegetation index (SAVI) [35], normalized difference built-up index (NDBI) [36], ratio vegetation index (RVI) [37], and modified normalized difference water index (MNDWI) [38].

**Table 4.** Formulas of spectral indices.

| Spectral Index | Formula | Application |
|---|---|---|
| NDVI | $\frac{NIR - R}{NIR + R}$ | Mainly used to detect vegetation cover and distinguish vegetation from non-vegetation |
| EVI | $2.5 \times \frac{NIR - R}{NIR + 6 \times R - 7.5 \times B + 1}$ | Good for detecting sparse vegetation |
| SAVI | $\frac{NIR - R}{NIR + R + L} \times (1 + L)$ | Reduces the effect of soil background and increases sensitivity to sparse vegetation |
| NDBI | $\frac{SWIR - NIR}{SWIR + NIR}$ | The value range is −1~1, and the value of artificial surfaces is greater than 0 |
| RVI | $\frac{NIR}{R}$ | A good reflection of the differences in vegetation growth status and coverage |
| MNDWI | $\frac{G - SWIR1}{G + SWIR1}$ | Good for distinguishing between water bodies and shadows |

However, the conventional vegetation indices still have limitations in distinguishing between evergreen and deciduous forests, and the phenological features extracted from the vegetation indices have been proven to be important in the fine classification of vegetation. To extract the phenological features, two-year time series curves of the three vegetation indices were constructed. However, the time series curves were inevitably affected by rain, ground ice, and snow; therefore, some abnormal values appeared, which greatly adversely affected the accuracy of the acquisition of phenological features. Finally, the harmonic analysis of time series (HANTS) method was used to remove the abnormal values and reconstruct the time series, making the curves smoother and more realistic to reflect the cyclical change patterns of vegetation growth [39]. Taking NDVI as an example, its original time series curve (blue curve) and reconstructed time series curve (red curve) are shown in Figure 4, where the X-axis represents the months.
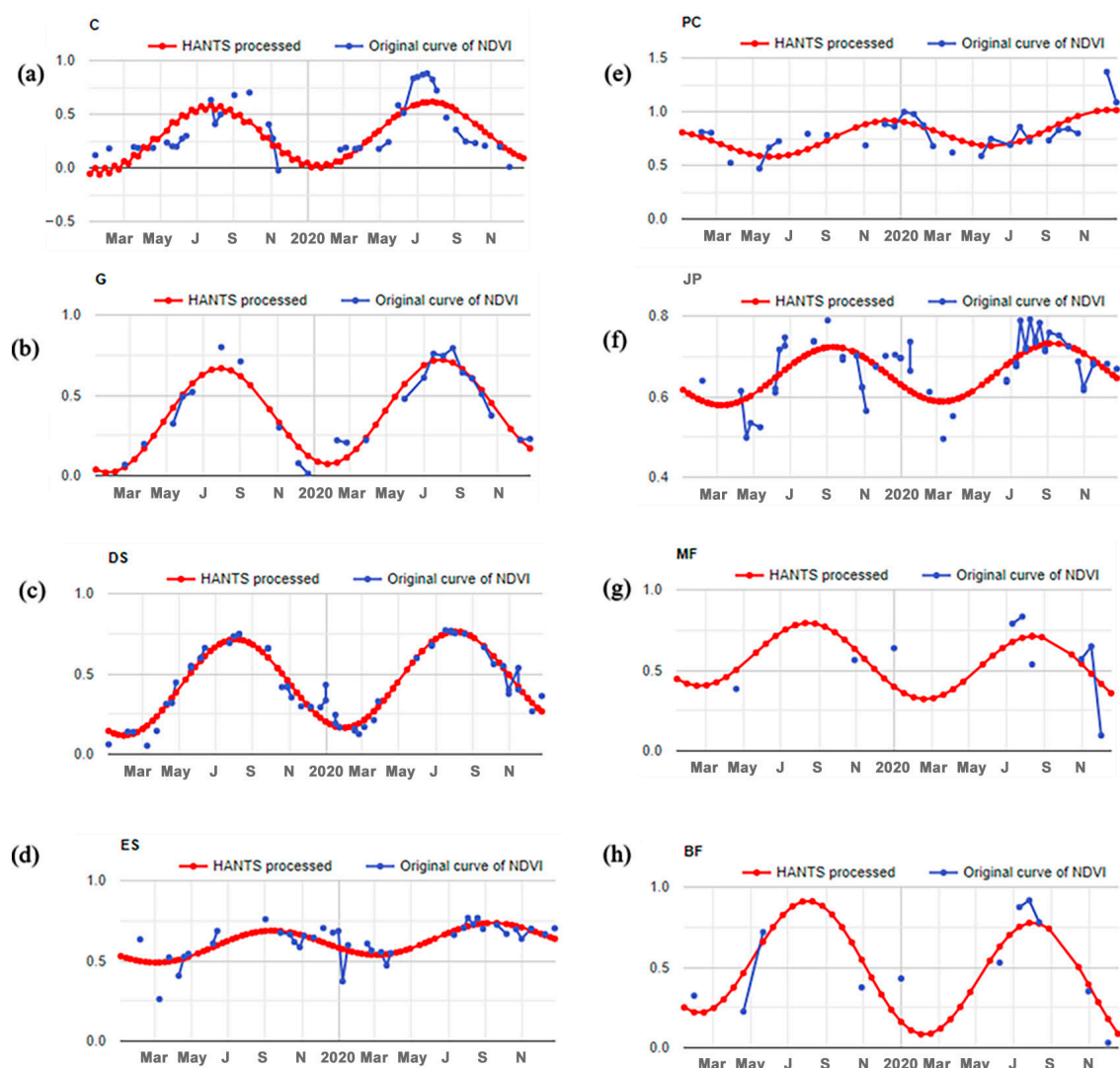
**Figure 4.** Reconstruction of NDVI time series curves: (**a**) cropland, (**b**) grassland, (**c**) deciduous shrub, (**d**) evergreen shrub, (**e**) *Picea crassifolia*, (**f**) *Juniperus przewalskii*, (**g**) mixed forest, and (**h**) broadleaf forest (meaning of the letters on the X-axis from left to right: Mar, March; May, May; J, July; S, September; N, November).

To better reflect the growth of vegetation in different periods, five parameters—the maximum value, minimum value, mean value, amplitude, and phase angle—of the three vegetation indices were extracted as features to participate in the classification. The final selection of all features is shown in Table 5.

**Table 5.** The feature parameters selected to participate in the classification.

| Type | Name | Parameters |
|---|---|---|
| Spectral | Landsat 5 and 7 bands | B1, B2, B3, B4, B5, B7 |
| | Landsat 8 bands | B2, B3, B4, B5, B6, B7 |
| | Tassel cap transformation | Brightness, greenness, wetness |
| | Spectral index | MNDWI, NDBI, RVI |
| | Phenological | NDVI_MIN, NDVI_MEAN, NDVI_MAX, magnitude, phase, EVI_MIN, EVI_MEAN, EVI_MAX, magnitude2, phase2, SAVI_MIN, SAVI_MEAN, SAVI_MAX, magnitude3, phase3 |
| Texture | Gray-level co-occurrence matrix (near-infrared) | B8(B5)_asm, B8(B5)_var, B8(B5)_idm, B8(B5)_ent, B8(B5)_contrast, B8(B5)_corr |
| Terrain | Terrain factors | SLOPE, ELEVATION, ASPECT, HILLSHADE |

### 2.4.2. Jeffries–Matusita Distance

The feature selection method based on Jeffries–Matusita (J-M) distance has been widely used in the study of remote sensing classification and is highly evaluated. For example, Pacheco et al. [40] used J-M distance to evaluate separability between burned and unburned vegetation. Thomas et al. [41] concluded that J-M distance is reliable in separability measurements and suitable for less homogeneous classes. Feature optimization based on the J-M distance method was implemented to reduce the computational complexity and improve the classification accuracy by removing redundancy from the existing features. The J-M distance is an important indicator of the separability of a single feature between categories; the principle is to calculate the sample distance between each category to determine the separability of the category and then select the features with high separability for similar land cover types [42]. It has been widely used, owing to its simple, efficient parameters and accurate optimization results, and its formula is expressed as follows:

$$JM = 2\left(1 - e^{-B}\right) \tag{1}$$

$$B = \frac{1}{8}(m_1 - m_2)^2 \frac{2}{\sigma_1{}^2 + \sigma_2{}^2} + \frac{1}{2}\ln\left[\frac{\sigma_1{}^2 + \sigma_2{}^2}{2\sigma_1\sigma_2}\right] \tag{2}$$

where B denotes the Bhattacharyya distance, and $m_i$ and $\sigma_i$ are the mean and variance of a feature of two different classes, respectively.

### 2.4.3. Sample Migration

The sample data in classification directly affect the accuracy of the classification results. In this study, an automated sampling method was used to obtain high-quality sample data, which significantly reduces the workload required to obtain reliable samples. First, a certain number of random points of various land cover types were generated using the FROM_GLC10 land cover product. Second, a preliminary sample set was formed by visual interpretation of high-resolution images on Google Earth supplemented by fieldwork sample points. Third, the classification was performed, and the sample set was corrected according to the confusion matrix of the classification and used as a reliable sample set for the reference year. Finally, the spectral angles of the same points in the target and reference years were measured based on the spectral angle mapping (SAM) method [43].

The principle of the SAM method is to treat the spectrum of each image element as a high-dimensional vector and measure the similarity between the spectra by calculating the angle between the two vectors. The smaller the angle between the two vectors, the more similar the spectra are and the more likely that they belong to the same species. Suitable thresholds can exclude pixels with a high probability of experiencing land cover

change, thereby providing a constant and high-quality training sample for the target year. Therefore, a trial-and-error procedure was used to find the optimal threshold, which was experimentally set to 0.2 to ensure sufficient high-quality samples for the target year. This method allowed for automatic updating of the sample set without fieldwork. The final sample size for each land cover type is shown in Table 6.

**Table 6.** Land cover samples in the study area based on sample migration.

| Year | 2020 | 2010 | 2000 | 1990 |
| --- | --- | --- | --- | --- |
| *Picea crassifolia* | 476 | 475 | 475 | 440 |
| Grassland | 1081 | 971 | 972 | 931 |
| Bare land | 902 | 771 | 669 | 729 |
| Water body | 61 | 24 | 24 | 16 |
| Impervious surface | 242 | 242 | 236 | 235 |
| Snow and ice | 119 | 67 | 26 | 49 |
| Cropland | 247 | 231 | 224 | 228 |
| *Juniperus przewalskii* | 146 | 146 | 146 | 146 |
| Deciduous shrub | 287 | 280 | 279 | 248 |
| Evergreen shrub | 149 | 119 | 140 | 20 |
| Mixed forest | 63 | 54 | 54 | 45 |
| Broadleaf forest | 118 | 118 | 113 | 104 |
| Total | 3891 | 3498 | 3358 | 3191 |

### 2.4.4. Classification and Accuracy Assessment

The random forest (RF) algorithm has shown good performance in land cover classification [19,44,45]. RF is an integrated classification algorithm that uses multiple decision trees to complete training and prediction [46]. The core of RF is integrated learning, which greatly compensates for the shortcomings caused by a single classifier. In the classification process, each decision tree acted as a basic unit to vote on the prediction of the sample, thereby improving the generalization ability of the algorithm and making the classification results more reliable.

The accuracy of the RF algorithm results depends largely on the number of decision trees. Therefore, to obtain more accurate classification results, in this study, we set the number of trees as 50, 100, 150, 200, 250, 300, 350, 400, 450, and 500 and compared the final classification accuracy. The results are shown in Figure 5. The results show that the overall classification accuracy increased with the number of decision trees until the maximum classification accuracy reached 400 and then remained stable, so the number of trees in the final random forest classifier was set to 400. In addition, the 10-fold cross-validation method can better train the RF classifier and verify its classification performance.

To evaluate the classification results for each year, in this study, we calculated four metrics based on the confusion matrix—the overall accuracy (OA), F1 score, producer accuracy (PA), and user accuracy (UA)—to objectively illustrate the accuracy of the classification [47,48]. The calculation formulas and descriptions are shown in Table 7.
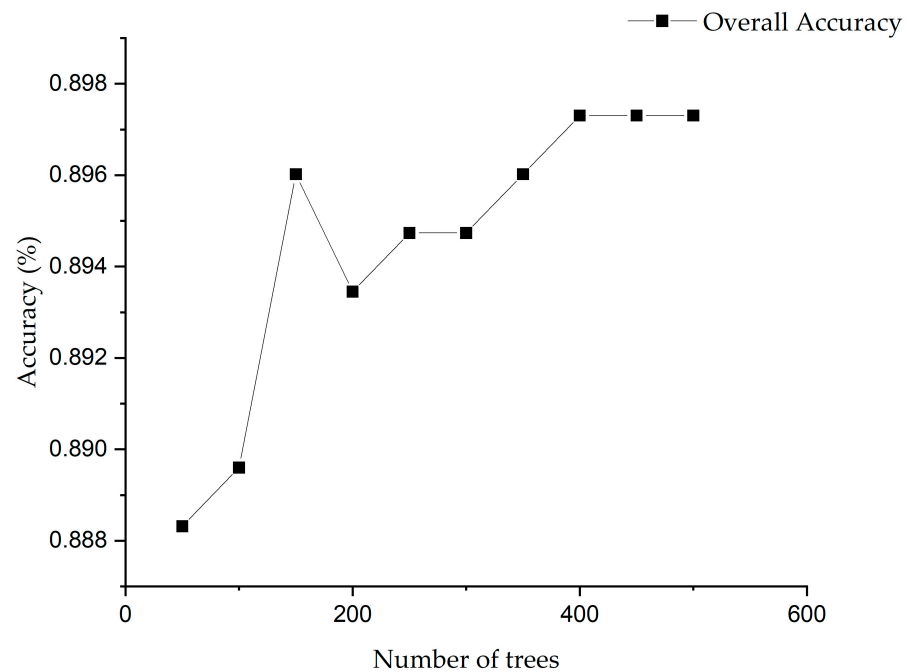
**Figure 5.** Variation in land cover classification accuracy with the number of decision trees.

**Table 7.** Evaluation indices of accuracy.

| Name | Formula | Description |
|---|---|---|
| Overall Accuracy | $\mathrm{OA} = \frac{\sum_{i=1}^{k} X_i}{N}$ | The number of correctly classified pixels divided by the total number of pixels |
| F1 Score | $\mathrm{F1} = \frac{2 \times p \times r}{p + r}$<br>$p = \frac{TP}{TP + FP}$<br>$r = \frac{TP}{TP + FN}$ | For a specific class A, *TP* is the number of pixels correctly classified as A, *FP* is the number of pixels incorrectly classified as A, *FN* is the number of pixels that A incorrectly classified as non-A, and TN is the number of pixels correctly classified as Non-A |
| User Accuracy | $\mathrm{UA} = \frac{X_i}{\sum_{i=1}^{r} X_i}$ | For a specific class (A), UA is the number of pixels correctly classified as A divided by the total number of pixels in class A |
| Producer Accuracy | $\mathrm{PA} = \frac{X_i}{\sum_{i=1}^{c} X_i}$ | For a specific class (A), PA is the number of pixels correctly classified as A divided by the number of all true pixels in class A |

## 3. Results

### 3.1. Optimization of Classification Features Based on the J-M Distance Method

All of the extracted features were used for land cover classification; the confusion matrix of the classification results through the Landsat 8 images in 2020 is presented in Table 8, showing that the easily confused land cover types include impervious surface and bare land, cropland and grassland, deciduous shrub and grassland, mixed coniferous forest and *Picea crassifolia*, and broadleaf forest and deciduous shrub.

**Table 8.** Confusion matrix for 2020 classification results obtained from samples of all land cover (LC) types (the unit of the data in the table is number of samples).

| LC Type | PC | G | BL | W | IS | SI | C | JP | DS | ES | MF | BF |
|---------|----|----|----|----|----|----|----|----|----|----|----|----|
| PC | 88 | 0 | 0 | 0 | 0 | 0 | 0 | 1 | 6 | 0 | 0 | 0 |
| G | 0 | 193 | 4 | 0 | 1 | 0 | 3 | 0 | 3 | 0 | 0 | 0 |
| BL | 0 | 3 | 174 | 0 | 2 | 0 | 0 | 0 | 0 | 0 | 0 | 0 |
| W | 0 | 0 | 0 | 13 | 0 | 0 | 0 | 0 | 0 | 0 | 0 | 0 |
| IS | 0 | 11 | 6 | 1 | 37 | 0 | 1 | 0 | 1 | 0 | 0 | 1 |
| SI | 0 | 0 | 2 | 0 | 0 | 25 | 0 | 0 | 0 | 0 | 0 | 0 |
| C | 0 | 11 | 0 | 0 | 1 | 0 | 38 | 0 | 1 | 0 | 0 | 2 |
| JP | 0 | 1 | 0 | 0 | 0 | 0 | 0 | 15 | 0 | 0 | 0 | 0 |
| DS | 0 | 8 | 0 | 0 | 0 | 0 | 2 | 0 | 44 | 1 | 0 | 0 |
| ES | 2 | 0 | 0 | 0 | 0 | 0 | 0 | 0 | 0 | 39 | 0 | 0 |
| MF | 3 | 0 | 0 | 0 | 0 | 0 | 0 | 1 | 0 | 0 | 12 | 0 |
| BF | 1 | 2 | 1 | 0 | 0 | 0 | 2 | 0 | 4 | 0 | 0 | 12 |

Since J-M distance can calculate the separability for two types of features, the J-M distances were calculated for the above five pairs of confusable land cover types, the results of which are shown in Figure 6. The higher the value of J-M distance, the better the separability of the feature to the pair of corresponding land types.
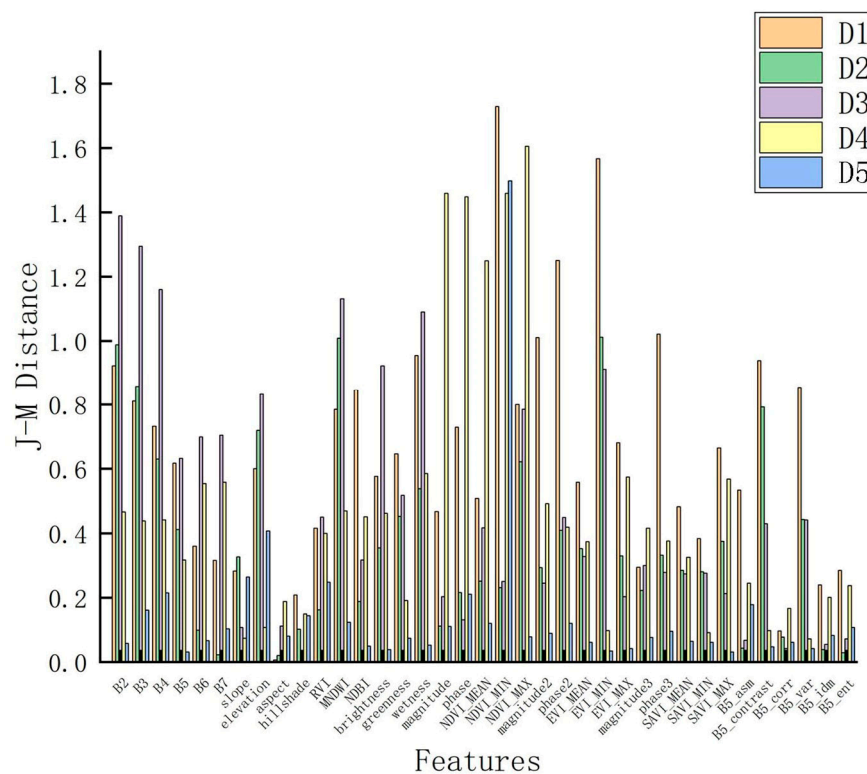
**Figure 6.** The J-M distance between different land cover types of Landsat 8 in 2020 (D1 indicates IS and BL, D2 indicates C and G, D3 indicates DS and G, D4 indicates MF and PC, and D5 indicates BF and DS).

The J-M distances of all features for each pair of land cover types were ranked from largest to smallest. As seen in Figure 6, for D1 and D5, the J-M distance of NDVI_MIN is the largest; for D2, the value of EVI_MIN is the largest; for D3, the value of B2 is the largest; and for D4, the value of NDVI_MAX is the largest. Therefore, these features were included in top combination in Table 9. Accordingly, the top ten and the first fifteen features were obtained, as shown in Table 9. NDBI and MNDWI were also included in the top combination, owing to their proven effectiveness in distinguishing impervious

surfaces from water bodies. These combinations of features were included in land cover classification; the variation in classification accuracy with different feature combinations is shown in Figure 7. The final classification features and detailed information are shown in Table 10.

**Table 9.** Classification features for 2020.

| Combination | Features |
|---|---|
| Top 1 | NDVI_MIN, EVI_MIN, B2, NDVI_MAX, NDBI, MNDWI |
| Top 2 | Top 1 + ELEVATION, B3 |
| Top 3 | Top 2 + phase2, B4, magnitude, SLOPE |
| Top 4 | Top 3 + RVI, phase, phase3 |
| Top 5 | Top 4 + magnitude2, B8_contrast, wetness, NDVI_MEAN |
| Top 6 | Top 5 + brightness |
| Top 7 | Top 6 + B8_asm, EVI_MAX |
| Top 8 | Top 7 + SAVI_MAX |
| Top 9 | Top 8 + B7, B8_var, HILLSHADE |
| Top 10 | Top 9 + B6, greenness |
| Top 15 | Top 10 + B5, B8_ent |
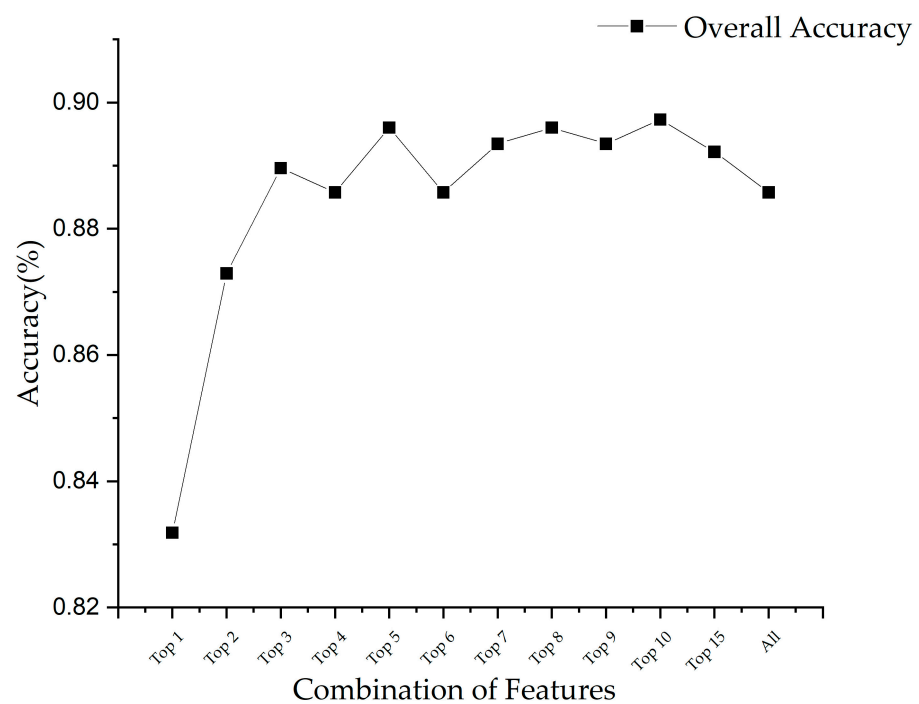
**Figure 7.** Variation in land cover classification accuracy with feature combinations.

**Table 10.** Final classification features.

| Dataset | Combination | Number | Name |
|---|---|---|---|
| Landsat 8 | Top 10 | 28 | NDVI_MIN, EVI_MIN, B2, NDVI_MAX, NDBI, MNDWI, ELEVATION, B3, phase2, B4, magnitude, SLOPE, RVI, phase, phase3, magnitude2, B8_contrast, wetness, NDVI_MEAN, brightness, B8_asm, EVI_MAX, SAVI_MAX, B7, B8_var, HILLSHADE, B6, greenness |

### 3.2. Land Cover Change in the QMNP from 1990 to 2020

Large changes in land cover every ten years between 1990 and 2020 are shown in the land cover transfer matrix in Tables 11–13, where PC, JP, MF, and BF were combined for forest (F), while DS and ES were combined for shrub (S), thereby highlighting the changes in forest, shrub, and grassland.

**Table 11.** Land transfer matrix for 1990–2000 (km$^2$).

|  | F | G | BL | W | IS | SI | C | S | Total Area in 2000 |
|---|---|---|---|---|---|---|---|---|---|
| F | 1520.2 | 73.0 | 54.3 | 2.7 | 1.7 | 0.0 | 0.6 | 190.1 | 1842.6 |
| G | 107.5 | 11,002.2 | 914.8 | 3.8 | 42.4 | 17.5 | 11.0 | 263.7 | 12,363.0 |
| BL | 6.3 | 904.4 | 29,951.5 | 69.6 | 16.1 | 381.2 | 3.9 | 16.8 | 31,349.8 |
| W | 0.5 | 0.9 | 164.2 | 21.2 | 0.1 | 3.1 | 0.0 | 0.4 | 190.4 |
| IS | 5.5 | 254.3 | 58.3 | 0.5 | 37.3 | 0.0 | 6.7 | 20.9 | 383.5 |
| SI | 0.0 | 42.1 | 277.0 | 1.2 | 0.0 | 1562.4 | 0.0 | 0.0 | 1882.7 |
| C | 0.5 | 8.9 | 2.0 | 0.0 | 4.1 | 0.0 | 26.9 | 2.8 | 45.2 |
| S | 286.2 | 572.8 | 43.1 | 4.2 | 3.1 | 0.1 | 1.7 | 1231.7 | 2142.8 |
| Total area in 1990 | 1926.6 | 12,858.5 | 31,465.3 | 103.2 | 104.6 | 1964.4 | 50.8 | 1726.5 | 50,200.0 |

**Table 12.** Transfer matrix of land cover for 2000–2010 (km$^2$).

|  | F | G | BL | W | IS | SI | C | S | Total Area in 2010 |
|---|---|---|---|---|---|---|---|---|---|
| F | 1489.8 | 137.8 | 8.9 | 1.4 | 5.4 | 0.0 | 0.7 | 215.2 | 1859.3 |
| G | 60.8 | 11,324.1 | 1623.7 | 2.2 | 238.7 | 53.1 | 13.2 | 374.5 | 13,690.2 |
| BL | 13.9 | 392.7 | 29,263.6 | 163.1 | 20.8 | 437.3 | 0.5 | 11.1 | 30,303.0 |
| W | 2.4 | 2.4 | 26.2 | 15.5 | 0.8 | 2.8 | 0.1 | 2.0 | 52.1 |
| IS | 14.1 | 86.9 | 97.7 | 1.0 | 98.1 | 0.0 | 6.9 | 26.6 | 331.3 |
| SI | 0.0 | 7.3 | 318.7 | 6.6 | 0.0 | 1389.5 | 0.0 | 0.0 | 1722.2 |
| C | 0.5 | 8.3 | 1.2 | 0.0 | 5.3 | 0.0 | 21.3 | 2.5 | 39.1 |
| S | 261.1 | 403.4 | 9.7 | 0.6 | 14.3 | 0.0 | 2.6 | 1510.8 | 2202.7 |
| Total area in 2000 | 1842.6 | 12,363.0 | 31,349.8 | 190.4 | 383.5 | 1882.7 | 45.2 | 2142.8 | 50,200.0 |

**Table 13.** Land transfer matrix for 2010–2020 (km$^2$).

|  | F | G | BL | W | IS | SI | C | S | Total Area in 2020 |
|---|---|---|---|---|---|---|---|---|---|
| F | 1549.6 | 54.7 | 31.5 | 1.2 | 17.6 | 0.0 | 2.6 | 207.4 | 1864.4 |
| G | 84.1 | 11,007.5 | 437.1 | 3.9 | 98.2 | 21.0 | 15.6 | 396.3 | 12,063.8 |
| BL | 25.2 | 1917.1 | 29,198.7 | 32.4 | 68.2 | 164.4 | 0.6 | 21.5 | 31,428.0 |
| W | 0.8 | 0.7 | 26.4 | 9.8 | 1.7 | 3.8 | 0.0 | 0.2 | 43.4 |
| IS | 10.5 | 294.4 | 91.4 | 0.5 | 126.6 | 0.0 | 4.7 | 13.5 | 541.7 |
| SI | 0.0 | 5.0 | 517.2 | 4.0 | 0.0 | 1533.0 | 0.0 | 0.0 | 2059.2 |
| C | 2.0 | 8.5 | 0.0 | 0.0 | 3.0 | 0.0 | 14.2 | 2.4 | 30.1 |
| S | 187.1 | 402.1 | 0.8 | 0.3 | 16.1 | 0.0 | 1.6 | 1561.3 | 2169.4 |
| Total area in 2010 | 1859.3 | 13,690.2 | 30,303.0 | 52.1 | 331.3 | 1722.2 | 39.1 | 2202.7 | 50,200.0 |

Table 11 shows that the conversion of forest to shrub and grassland from 1990 to 2000 was 286.2 and 107.5 km$^2$, respectively, while 904.4 km$^2$ of grassland was converted to bare land. The conversion of shrubland to grassland and forest was larger, with 263.7 km$^2$ converted to grassland and 190.1 km$^2$ converted to forest. In general, the area of forest and grassland decreased from 1990 to 2000, while the area of shrub increased, and the total area of vegetation slightly decreased.

Table 12 shows that the largest areas of forest converted to other features in 2000–2010 were shrub and grassland, with 261.1 km$^2$ and 60.8 km$^2$, respectively, both of which declined compared to 1990–2000. At the same time, a larger portion of bare land was converted to grassland. Overall, the areas of forest, shrub, and grassland increased, while the area of bare land decreased.

Table 13 shows that the area of forests increased, while the area of shrub and grassland slightly decreased from 2010 to 2020. There was little change in forest, and 1917.1 km² of grassland area was converted to bare land; 396.3 km² and 207.4 km² of shrub area were converted to grassland and forest, respectively. The total area of vegetation showed a decreasing trend, primarily due to the reduction in grassland.

It can be seen from Tables 11–13 that there were variations in forest, shrub, and grassland in every decade, but the total area of forest and scrub did not change considerably in any decade, which shows that vegetation cover change in mountainous areas is relatively slow. Moreover, the forest area decreased from 1990 to 2000 and gradually increased after 2000, which is also related to the implementation of a stricter ecological protection policy in QMNP in 2000.

To clearly indicate changes in forest, shrub, and grassland, QMNP was divided into 502 grids with a resolution of 10 km × 10 km, and their kernel density was estimated, as shown in Figure 8. The map of the (a) series in Figure 8 shows the spatial distribution of forest, shrub, and grassland changes every ten years between 1990 and 2020, and the map of the (b), (c), and (d) series in Figure 8 shows the kernel density estimates for forest, shrub, and grassland changes every ten years between 1990 and 2020.

The conversion between vegetation was noticeable from 1990 to 2000. Forest change was evident in the eastern and central parts of QMNP, mainly in Sunan and Tianzhu counties. Grassland also changed significantly in the eastern and central regions of the park, mainly in Subei and Tianjun counties. Shrub change areas cover a considerably wider range of the park, with a few areas in the west and more significant changes in the east and central parts. The conversion trends of forest, shrub, and grassland during the 2000–2010 and 2010–2020 periods were similar to those of 1990–2000.
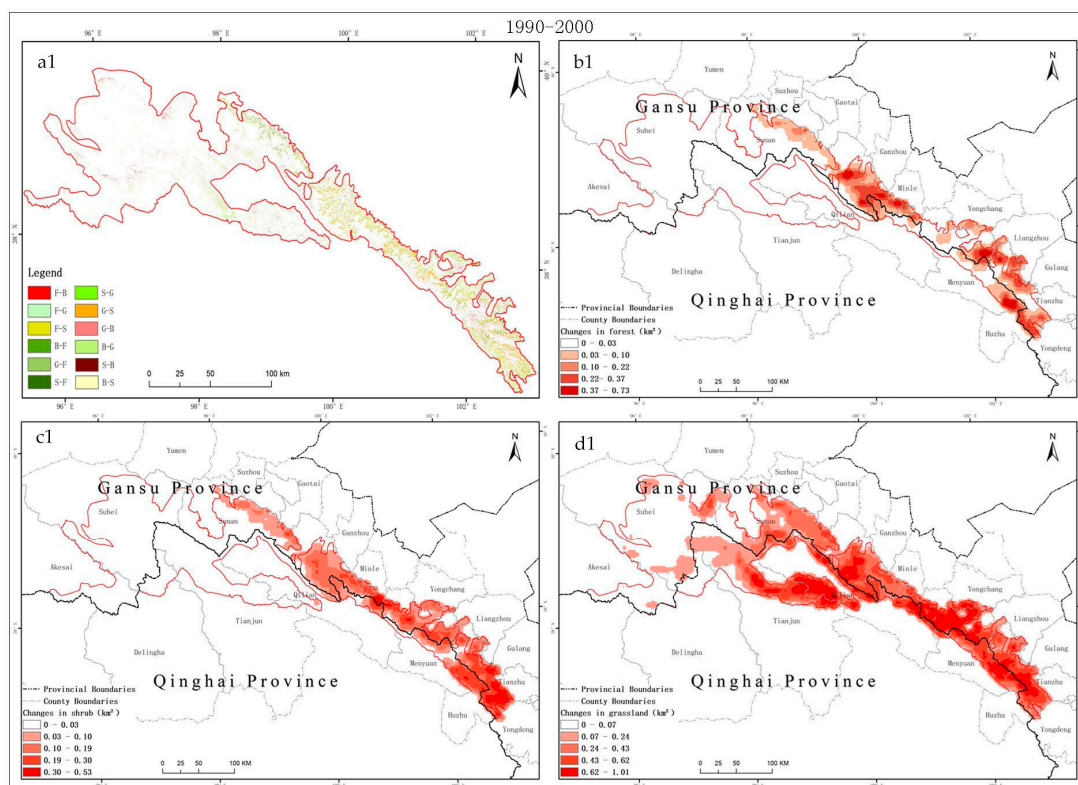
**Figure 8.** *Cont.*
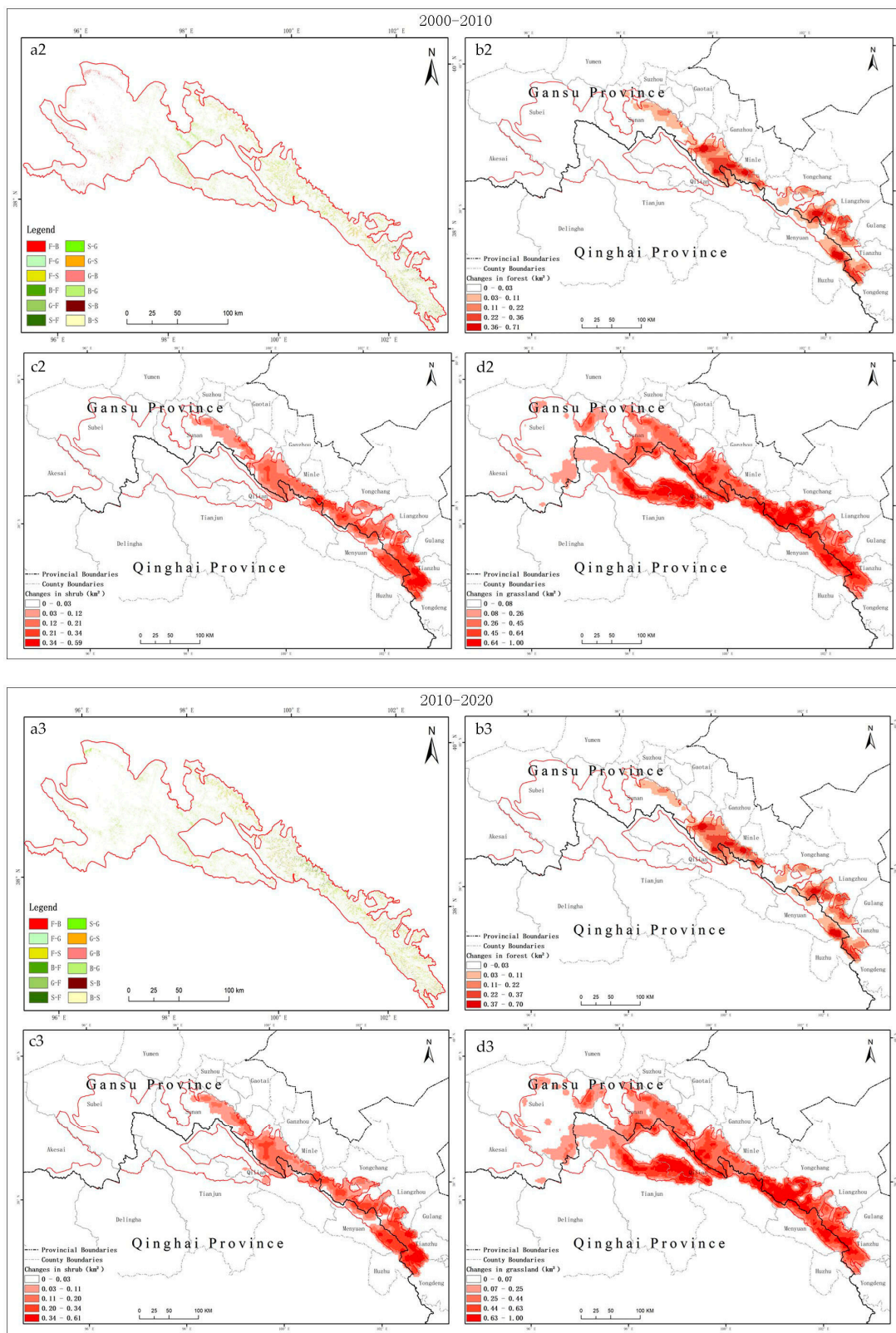
**Figure 8.** Changes in each decade from 1990 to 2020: series (**a1**–**a3**) spatial distribution of forest, shrub and grassland changes; series (**b1**–**b3**), series (**c1**–**c3**), series (**d1**–**d3**) kernel density estimates of forest, shrub, and grassland area changes.

The result of the land cover classification of QMNP in 2020 is shown in Figure 9. The vegetation varies strongly from east to west in QMNP. Forests are widely distributed in the central county of Sunan and the eastern county of Tianzhu. The spatial distribution of shrubs is the same as that of forest, and grassland is distributed in the central counties of Sunan and Qilian and the eastern county of Tianzhu, while bare land—the largest land cover type in QMNP—is concentrated in the western part of the national park. Regions A and B in Figure 9 belong to Sunan and Menyuan counties, respectively, where forests are abundantly distributed. Both Sunan and Menyuan counties have a large distribution of forests and contain several typical land cover types, such as Picea crassifolia, Juniperus przewalskii, evergreen shrub, deciduous shrub, and mixed forests.
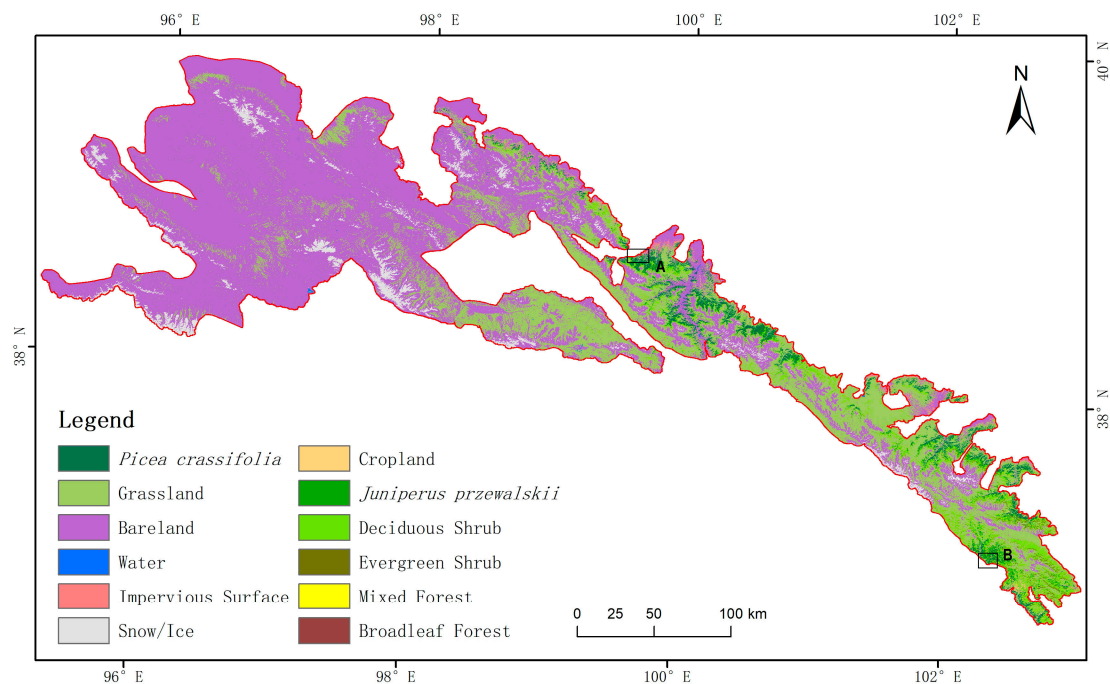
**Figure 9.** Land cover classification result for 2020.

Sunan and Menyuan counties were chosen for detailed demonstrations of vegetation changes because of the notable land cover changes, as shown in Figures 10 and 11. Figure 10 shows that the area of Sunan county mainly changed from forest to shrub during the 1990–2000 period, while the area was mainly converted from shrub to grassland during the 2010–2020 period. The changes were diverse during the 2000–2010 period. As shown in Figure 11, in Menyuan county, the conversion of forest to shrub occurred primarily during the 1990–2000 period, while other land cover types were converted to forest during the 2000–2010 period, and the conversion to forest was more notable during the 2010–2020 period.
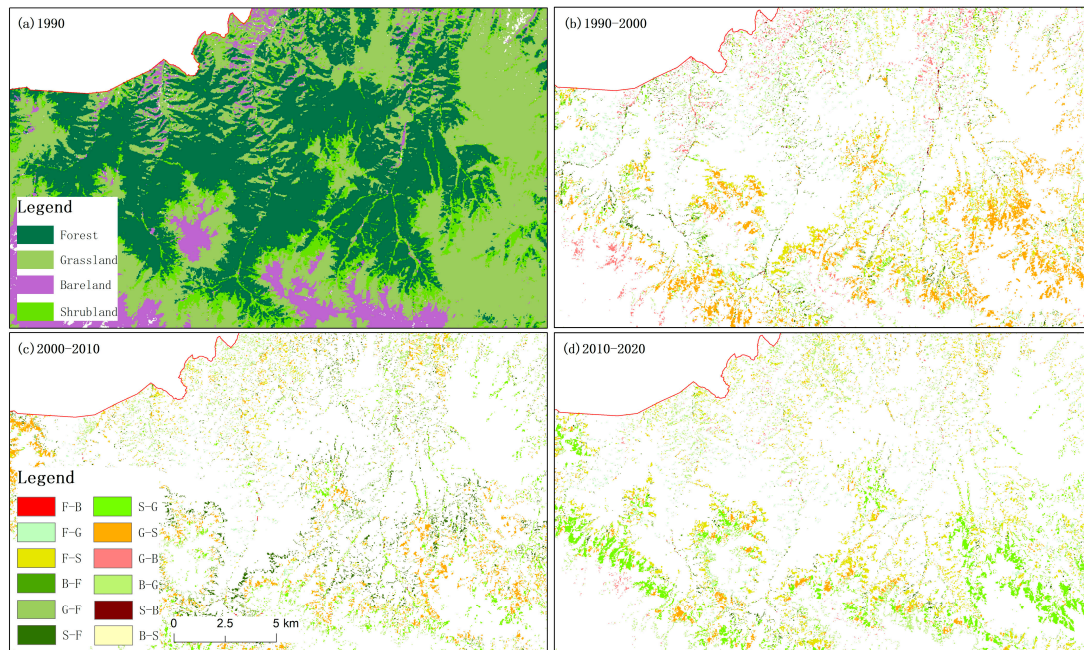
**Figure 10.** Detailed map of forest, shrub, and grassland changes in Sunan county: (**a**) spatial distribution of forest, shrub, grassland and bare land in 1990; (**b–d**) the changes of spatial distribution of forest, shrub, grassland and bare land in 1990–2000, 2000–2010 and 2010–2020, respectively.
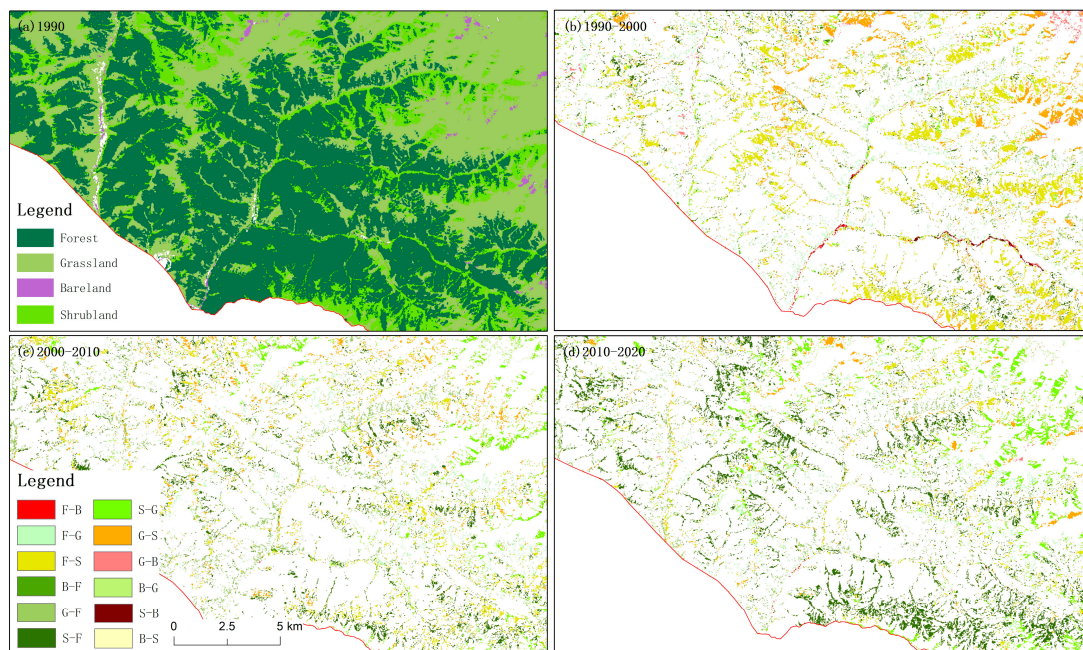
**Figure 11.** Detailed map of forest, shrub, and grassland changes in Menyuan county: (**a**) spatial distribution of forest, shrub, grassland and bare land in 1990; (**b–d**) the changes of spatial distribution of forest, shrub, grassland and bare land in 1990–2000, 2000–2010 and 2010–2020, respectively.

### 3.3. Accuracy of Land Cover Classification

The 10-fold cross-validation method was used for accuracy evaluation, which can avoid contingency in the result validation process and improve accuracy evaluation. All samples were divided into ten subsets, nine of which were used as training data and one as

validation data to perform classification, with the mean value of the results taken as the result of accuracy evaluation, as shown in Table 14.

**Table 14.** Accuracy evaluation of land cover classification results.

| Type | 1990 | | | | 2000 | | | | 2010 | | | | 2020 | | | |
|---|---|---|---|---|---|---|---|---|---|---|---|---|---|---|---|---|
| | PA (%) | UA (%) | Error | F1 Score | PA (%) | UA (%) | Error | F1 Score | PA (%) | UA (%) | Error | F1 Score | PA(%) | UA (%) | Error | F1 Score |
| PC | 0.900 | 0.914 | −0.014 | 0.907 | 0.914 | 0.932 | −0.018 | 0.923 | 0.938 | 0.930 | 0.008 | 0.934 | 0.937 | 0.953 | −0.016 | 0.945 |
| G | 0.845 | 0.932 | −0.087 | 0.886 | 0.869 | 0.945 | −0.076 | 0.905 | 0.879 | 0.946 | −0.067 | 0.911 | 0.894 | 0.946 | −0.052 | 0.919 |
| BL | 0.944 | 0.949 | −0.005 | 0.946 | 0.959 | 0.946 | 0.013 | 0.952 | 0.960 | 0.963 | −0.003 | 0.961 | 0.947 | 0.963 | −0.016 | 0.955 |
| W | 0.953 | 0.965 | −0.012 | 0.959 | 0.967 | 0.942 | 0.025 | 0.954 | 0.900 | 0.937 | −0.037 | 0.918 | 0.976 | 0.976 | 0 | 0.976 |
| IS | 0.812 | 0.823 | −0.011 | 0.817 | 0.790 | 0.789 | 0.001 | 0.789 | 0.793 | 0.815 | −0.022 | 0.804 | 0.861 | 0.833 | 0.028 | 0.847 |
| SI | 0.861 | 0.884 | −0.023 | 0.872 | 0.984 | 0.969 | 0.015 | 0.976 | 0.967 | 0.896 | 0.071 | 0.930 | 0.962 | 0.907 | 0.055 | 0.934 |
| C | 0.824 | 0.808 | 0.016 | 0.816 | 0.819 | 0.848 | −0.029 | 0.833 | 0.853 | 0.859 | −0.006 | 0.856 | 0.798 | 0.804 | −0.006 | 0.801 |
| JP | 0.898 | 0.850 | 0.048 | 0.873 | 0.874 | 0.844 | 0.03 | 0.859 | 0.908 | 0.903 | 0.005 | 0.905 | 0.935 | 0.941 | −0.006 | 0.938 |
| DS | 0.802 | 0.798 | 0.004 | 0.800 | 0.820 | 0.785 | 0.035 | 0.802 | 0.779 | 0.813 | −0.034 | 0.796 | 0.800 | 0.866 | −0.066 | 0.832 |
| ES | 0.834 | 0.825 | 0.009 | 0.829 | 0.810 | 0.874 | −0.064 | 0.841 | 0.842 | 0.903 | −0.061 | 0.871 | 0.892 | 0.926 | −0.034 | 0.909 |
| MF | 0.786 | 0.797 | −0.011 | 0.791 | 0.771 | 0.786 | −0.015 | 0.778 | 0.780 | 0.801 | −0.021 | 0.790 | 0.813 | 0.825 | −0.012 | 0.819 |
| BF | 0.814 | 0.803 | 0.011 | 0.808 | 0.805 | 0.815 | −0.01 | 0.810 | 0.831 | 0.826 | 0.005 | 0.828 | 0.806 | 0.801 | 0.005 | 0.803 |
| OA(%) | 0.839 | | | | 0.860 | | | | 0.880 | | | | 0.897 | | | |

Table 14 shows that the classification accuracy of land cover in all four periods was greater than 0.80, and the accuracy gradually increased from 1990 to 2020. The highest classification accuracy was 0.897 in 2020. The user and producer accuracy of each land cover type show that *Picea crassifolia*, grassland, bare land, water body, and *Juniperus przewalskii* had good classification accuracy in these four years, while the classification accuracy of deciduous shrubland, mixed forest, and broadleaf forest was slightly poorer, mainly due to the similarity of their spectral characteristics to those of other land cover types. The error values presented in the table were obtained by subtracting the UA from the PA of each land cover type. The F-scores of *Picea crassifolia*, grassland, bare land, and water bodies are almost all above 0.9 and are higher than the values of other land cover types, indicating better classification performance for these land cover types.

## 4. Discussion

The method combining phenological features, J-M distance, and sample migration provided time series land cover classification data in QMNP from 1990 to 2020; however, there are still some problems to be solved in the classification work. The lack of quality and auxiliary data in land cover classification is a serious issue in mountainous areas in the QMNP of Northwest China. Although remote sensing images can be filtered by the declouding algorithm of GEE, images in QMNP are affected by cloud cover, resulting in a lack of high-quality image sets [49]. For example, in the western part of QMNP, the selection of sample points for specific vegetation types may have been misjudged due to a lack of high-quality images, thereby affecting the final classification results [50]. To improve the classification of vegetation subdivision types, phenological features were extracted from the NDVI, EVI, and SAVI time series curves to participate in the classification, which can better reflect the seasonal differences in vegetation, especially for complex vegetation types in mountainous areas [16]. Elevation and phenological features showed good separability among easily confused feature classes based on J-M distance, especially among different vegetation types. In addition, in this study, we migrated the sample set based on the spectral angular distance in 2020 on the GEE. The final accuracy assessment demonstrates the feasibility of automatically acquiring samples with this method. It avoids the misjudgment of human visual judgment while greatly saving time and is especially suitable for mountainous regions where high-resolution data are lacking [51].

In the classification results, multisource datasets were used, and images with the least amount of clouds in the study area were provided, allowing for improved classification

accuracy. The field samples provide accurate land cover types, increasing the reliability of the samples, which is also the basis for sample migration and classification of images from other years. Since different features have different degrees of separation of land cover types, the phenological features in particular can better distinguish deciduous and evergreen forests, which greatly improves the accuracy of vegetation classification. Therefore, feature selections and optimizations were performed.

In addition, a comparison of Figures 5 and 7 shows that the effect of different numbers of trees on OA in random forest is much less than the effect of different feature combinations. The range of OA variation shown in Figure 5 is less than 1%, while the maximum difference of the effect of feature combinations on accuracy shown in Figure 7 is close to 9%. This result is reasonable, and the reason for such a strong variation is that the importance of feature selection is much higher than the importance of the number of trees in RF. Because the number of trees only affects the lower limit of classification accuracy when the classification features and samples are determined, whereas the upper limit is saturated when the number of trees sufficient. In contrast, the selection of classification features directly affects the upper limit of classification accuracy, and suitable classification features such as phenological features are effective means to distinguish evergreen species from deciduous species.

Exploring land cover dynamics is crucial for understanding ecological conservation in QMNP. The above results show generally trends that are generally consistent trends with the literature cited hereafter. Qian et al. [52] found that the land cover of the Qilian Mountain National Nature Reserve (QMNNR) has changed dramatically over the past four decades and that the land cover structure of the QMNNR has remained stable, although the total area of vegetation decreased by 49.6 km$^2$ from 1975 to 2015. Peng et al. [53] found that, with the majority of vegetation recovering significantly, only 0.14% of the QMNP area experienced significant degradation between 2000 and 2019. The height feature for vegetation structure, which can accurately distinguish shrubs and forests, is the primary difference between the two. However, there is a lack of auxiliary data that can reflect vegetation height information. Due to the lack of characteristics reflecting vegetation height information, future studies will concentrate on adding satellite-based vegetation height data to participate in classification to further improve the accuracy of forest and shrub classification.

## 5. Conclusions

A long time series of land cover data is considered to be a foundation for forest management and vegetation restoration in QMNP. Based on the GEE cloud platform and a reliable reference year sample dataset, in this study, we constructed a method to accomplish land cover classification using sample migration, avoiding complicated processing. The final classification was completed using the random forest algorithm, and good classification accuracy was achieved. To ensure accuracy and avoid bias of the samples, 500 random samples were generated for each classification type, and the correctly classified samples were retained by visual interpretation of Google Earth images. Fieldwork was conducted in multiyear scientific investigations to ensure an accurate and representative sample set. All the above efforts can be evenly distributed spatially to ensure better accuracy of the final classification.

For the QMNP as a whole, the results show that the total sample size decreased by 10.1%, 13.7%, and 18.0% when the 2020 sample was migrated to 2010, 2000, and 1990, respectively, and the overall precision reached 89.7%, 88.0%, 86.0%, and 83.9%, respectively. The feature set can be optimized well using the J-M distance, with 35 features reduced to 29 and overall accuracy improved from 88.6% to 89.7%. Analysis of land cover change in QMNP showed that vegetation changes were mainly accounted for by interconversion between forest, shrub, and grassland and that the areas of change were mainly distributed in Sunan and Tianzhu counties of Gansu Province and Menyuan county of Qinghai Province. Forests and shrubs were mainly distributed in Sunan and Tianzhu counties; forest decreased

by 62.2 km$^2$ and shrub increased by 442.9 km$^2$ from 1990 to 2020. Grasslands are abundantly distributed mainly in Sunan, Qilian, and Tianzhu counties and decreased by 794.7 km$^2$ from 1990 to 2020.

The results of land cover change can reveal which areas of the QMNP have experienced the greatest changes in vegetation coverage such as forest and scrub so that efforts can be focused on the conservation of these areas. Therefore, it makes sense for regional management protection. In addition, this study can be considered to provide a framework for research on land cover change. Accordingly, for any other mountainous region in the world, land cover change can be determined using the research framework proposed in this paper as long as sample and image data are available for that particular region.

**Author Contributions:** Y.N. designed the method and technological procedure. Y.N. and Z.H. wrote the majority of the paper. W.Z. edited the rest of the paper. L.C. provided the elevation distribution data of different cover types in Table 1. All authors have read and agreed to the published version of the manuscript.

**Funding:** This research was supported by the Second Tibetan Plateau Scientific Expedition and Research Program (STEP) (grant number 2019QZKK0301) and the National Key R&D Program of China (grant number 2019YFC0507401).

**Data Availability Statement:** Data will be available from corresponding authors upon reasonable request.

**Acknowledgments:** We sincerely thank the anonymous reviewers for their valuable comments.

**Conflicts of Interest:** The authors declare no conflict of interest.

## References

1. Findell, K.L.; Berg, A.; Gentine, P.; Krasting, J.P.; Lintner, B.R.; Malyshev, S.; Santanello, J.A.; Shevliakova, E. The Impact of Anthropogenic Land Use and Land Cover Change on Regional Climate Extremes. *Nat. Commun.* **2017**, *8*, 989. [CrossRef] [PubMed]
2. Sun, C.; Liu, Y.; Song, H.; Li, Q.; Cai, Q.; Wang, L.; Fang, C.; Liu, R. Tree-Ring Evidence of the Impacts of Climate Change and Agricultural Cultivation on Vegetation Coverage in the Upper Reaches of the Weihe River, Northwest China. *Sci. Total Environ.* **2020**, *707*, 136160. [CrossRef]
3. Yan, K.; Ding, Y. The Overview of the Progress of Qilian Mountain National Park System Pilot Area. *Int. J. Geoheritage Park.* **2020**, *8*, 210–214. [CrossRef]
4. Galacho-Jiménez, F.B.; Quesada-Molina, P.; Carruana-Herrera, D.; Reyes-Corredera, S. Application of the Analysis Time Series and Multispectral Images for the Estimation of the Conditions of the Vegetation Covers of the Natural Areas of Southern Spain. *Land* **2022**, *12*, 42. [CrossRef]
5. Zongxing, L.; Qi, F.; Zongjie, L.; Xufeng, W.; Juan, G.; Baijuan, Z.; Yuchen, L.; Xiaohong, D.; Jian, X.; Wende, G.; et al. Reversing Conflict between Humans and the Environment—The Experience in the Qilian Mountains. *Renew. Sustain. Energy Rev.* **2021**, *148*, 111333. [CrossRef]
6. Chagas, V.B.P.; Chaffe, P.L.B.; Blöschl, G. Climate and Land Management Accelerate the Brazilian Water Cycle. *Nat. Commun.* **2022**, *13*, 5136. [CrossRef] [PubMed]
7. Gong, P.; Liu, H.; Zhang, M.; Li, C.; Wang, J.; Huang, H.; Clinton, N.; Ji, L.; Li, W.; Bai, Y.; et al. Stable Classification with Limited Sample: Transferring a 30-m Resolution Sample Set Collected in 2015 to Mapping 10-m Resolution Global Land Cover in 2017. *Sci. Bull.* **2019**, *64*, 370–373. [CrossRef]
8. Yu, W.J.; Zhou, W.Q.; Qian, Y.G.; Yan, J.L. A New Approach for Land Cover Classification and Change Analysis: Integrating Backdating and an Object-Based Method. *Remote Sens. Environ.* **2016**, *177*, 37–47. [CrossRef]
9. Lu, M.; Chen, J.; Tang, H.J.; Rao, Y.H.; Yang, P.; Wu, W.B. Land Cover Change Detection by Integrating Object-Based Data Blending Model of Landsat and MODIS. *Remote Sens. Environ.* **2016**, *184*, 374–386. [CrossRef]
10. Aguirre-Gutierrez, J.; Seijmonsbergen, A.C.; Duivenvoorden, J.F. Optimizing Land Cover Classification Accuracy for Change Detection, a Combined Pixel-Based and Object-Based Approach in a Mountainous Area in Mexico. *Appl. Geogr.* **2012**, *34*, 29–37. [CrossRef]
11. Tehrany, M.S.; Pradhan, B.; Jebuv, M.N. A Comparative Assessment between Object and Pixel-Based Classification Approaches for Land-Use/Land-Cover Mapping Using SPOT 5 Imagery. *Geocarto Int.* **2014**, *29*, 351–369. [CrossRef]
12. Phiri, D.; Morgenroth, J. Developments in Landsat Land Cover Classification Methods: A Review. *Remote Sens.* **2017**, *9*, 967. [CrossRef]
13. Gorelick, N.; Hancher, M.; Dixon, M.; Ilyushchenko, S.; Thau, D.; Moore, R. Google Earth Engine: Planetary-Scale Geospatial Analysis for Everyone. *Remote Sens. Environ.* **2017**, *202*, 18–27. [CrossRef]

14. Reed, B.C.; Brown, J.F.; Vanderzee, D.; Loveland, T.R.; Merchant, J.W.; Ohlen, D.O. Measuring Phenological Variability from Satellite Imagery. *J. Veg. Sci.* **1994**, *5*, 703–714. [CrossRef]

15. Nguyen, L.H.; Joshi, D.R.; Clay, D.E.; Henebry, G.M. Characterizing Land Cover/Land Use from Multiple Years of Landsat and MODIS Time Series: A Novel Approach Using Land Surface Phenology Modeling and Random Forest Classifier. *Remote Sens. Environ.* **2020**, *238*, 1677. [CrossRef]

16. Zeng, L.L.; Wardlow, B.D.; Xiang, D.X.; Hu, S.; Li, D.R. A Review of Vegetation Phenological Metrics Extraction Using Time-Series, Multispectral Satellite Data. *Remote Sens. Environ.* **2020**, *237*, 111511. [CrossRef]

17. Huang, H.B.; Chen, Y.L.; Clinton, N.; Wang, J.; Wang, X.Y.; Liu, C.X.; Gong, P.; Yang, J.; Bai, Y.Q.; Zheng, Y.M.; et al. Mapping Major Land Cover Dynamics in Beijing Using All Landsat Images in Google Earth Engine. *Remote Sens. Environ.* **2017**, *202*, 166–176. [CrossRef]

18. Naboureh, A.; Li, A.N.; Ebrahimy, H.; Bian, J.H.; Azadbakht, M.; Amani, M.; Lei, G.B.; Nan, X. Assessing the Effects of Irrigated Agricultural Expansions on Lake Urmia Using Multi-Decadal Landsat Imagery and a Sample Migration Technique within Google Earth Engine. *Int. J. Appl. Earth Obs. Geoinf.* **2021**, *105*, 102607. [CrossRef]

19. Ghorbanian, A.; Kakooei, M.; Amani, M.; Mahdavi, S.; Mohammadzadeh, A.; Hasanlou, M. Improved Land Cover Map of Iran Using Sentinel Imagery within Google Earth Engine and a Novel Automatic Workflow for Land Cover Classification Using Migrated Training Samples. *Isprs J. Photogramm Remote Sens.* **2020**, *167*, 276–288. [CrossRef]

20. Huang, H.B.; Wang, J.; Liu, C.X.; Liang, L.; Li, C.C.; Gong, P. The Migration of Training Samples towards Dynamic Global Land Cover Mapping. *ISPRS J. Photogramm.* **2020**, *161*, 27–36. [CrossRef]

21. Liu, H.; Gong, P.; Wang, J.; Wang, X.; Ning, G.; Xu, B. Production of Global Daily Seamless Data Cubes and Quantification of Global Land Cover Change from 1985 to 2020-IMap World 1.0. *Remote Sens. Environ.* **2021**, *258*, 112364. [CrossRef]

22. Zhong, B.; Yang, A.X.; Jue, K.S.; Wu, J.J. Long Time Series High-Quality and High-Consistency Land Cover Mapping Based on Machine Learning Method at Heihe River Basin. *Remote Sens.* **2021**, *13*, 1596. [CrossRef]

23. Li, C.; Zou, Y.Y.; He, J.F.; Zhang, W.; Gao, L.L.; Zhuang, D.F. Response of Vegetation Phenology to the Interaction of Temperature and Precipitation Changes in Qilian Mountains. *Remote Sens.* **2022**, *14*, 1248. [CrossRef]

24. Wang, W.; He, Z.B.; Du, J.; Ma, D.K.; Zhao, P. Altitudinal Patterns of Species Richness and Flowering Phenology in Herbaceous Community in Qilian Mountains of China. *Int. J. Biometeorol.* **2022**, *66*, 741–751. [CrossRef]

25. Fang, J.; Tian, Q.Y.; He, Z.B.; Du, J.; Chen, L.F.; Lin, P.F.; Zhu, X. Response of Sap Flow in Qinghai Spruce (*Picea crassifolia*) to Environmental Variables in the Qilian Mountains of China. *Trees* **2022**, *36*, 1261–1272. [CrossRef]

26. Li, J.C.; Pang, G.J.; Wang, X.J.; Liu, F.; Zhang, Y.T. Spatiotemporal Dynamics of Land Surface Albedo and Its Influencing Factors in the Qilian Mountains, Northeastern Tibetan Plateau. *Remote Sens.* **2022**, *14*, 1922. [CrossRef]

27. Masek, J.G.; Vermote, E.F.; Saleous, N.E.; Wolfe, R.; Hall, F.G.; Huemmrich, K.F.; Gao, F.; Kutler, J.; Lim, T.K. A Landsat Surface Reflectance Dataset for North America, 1990–2000. *IEEE Geosci. Remote Sens. Lett.* **2006**, *3*, 68–72. [CrossRef]

28. Foga, S.; Scaramuzza, P.L.; Guo, S.; Zhu, Z.; Dilley, R.D.; Beckmann, T.; Schmidt, G.L.; Dwyer, J.L.; Hughes, M.J.; Laue, B. Cloud Detection Algorithm Comparison and Validation for Operational Landsat Data Products. *Remote Sens. Environ.* **2017**, *194*, 379–390. [CrossRef]

29. Senf, C. Seeing the System from Above: The Use and Potential of Remote Sensing for Studying Ecosystem Dynamics. *Ecosystems* **2022**, *25*, 1719–1737. [CrossRef]

30. Haralick, R.M.; Shanmugam, K.; Dinstein, I. Textural Features for Image Classification. *IEEE Trans. Syst. Man Cybern.* **1973**, *SMC-3*, 610–621. [CrossRef]

31. Lu, D.; Weng, Q. A Survey of Image Classification Methods and Techniques for Improving Classification Performance. *Int. J. Remote Sens.* **2007**, *28*, 823–870. [CrossRef]

32. Crist, E.P.; Cicone, R.C. A Physically-Based Transformation of Thematic Mapper Data—The TM Tasseled Cap. *IEEE Trans. Geosci. Remote* **1984**, *22*, 256–263. [CrossRef]

33. Goward, S.N.; Markham, B.; Dye, D.G.; Dulaney, W.; Yang, J. Normalized Difference Vegetation Index Measurements from the Advanced Very High Resolution Radiometer. *Remote Sens. Environ.* **1991**, *35*, 257–277. [CrossRef]

34. Jiang, Z.Y.; Huete, A.R.; Didan, K.; Miura, T. Development of a Two-Band Enhanced Vegetation Index without a Blue Band. *Remote Sens. Environ.* **2008**, *112*, 3833–3845. [CrossRef]

35. Huete, A.R. A Soil-Adjusted Vegetation Index (SAVI). *Remote Sens. Environ.* **1988**, *25*, 295–309. [CrossRef]

36. Zhang, Y.S.; Odeh, I.O.A.; Han, C.F. Bi-Temporal Characterization of Land Surface Temperature in Relation to Impervious Surface Area, NDVI and NDBI, Using a Sub-Pixel Image Analysis. *Int. J. Appl. Earth Obs. Geoinf.* **2009**, *11*, 256–264. [CrossRef]

37. Major, D.J.; Baret, F.; Guyot, G. A Ratio Vegetation Index Adjusted for Soil Brightness. *Int. J. Remote Sens.* **1990**, *11*, 727–740. [CrossRef]

38. Xu, H.Q. Modification of Normalised Difference Water Index (NDWI) to Enhance Open Water Features in Remotely Sensed Imagery. *Int. J. Remote Sens.* **2006**, *27*, 3025–3033. [CrossRef]

39. Zhou, J.; Jia, L.; Menenti, M. Reconstruction of Global MODIS NDVI Time Series: Performance of Harmonic ANalysis of Time Series (HANTS). *Remote Sens. Environ.* **2015**, *163*, 217–228. [CrossRef]

40. Pacheco, A.D.P.; Junior, J.A.D.S.; Ruiz-Armenteros, A.M.; Henriques, R.F.F. Assessment of K-Nearest Neighbor and Random Forest Classifiers for Mapping Forest Fire Areas in Central Portugal Using Landsat-8, Sentinel-2, and Terra Imagery. *Remote Sens.* **2021**, *13*, 1345. [CrossRef]

41. Thomas, I.L.; Ching, N.P.; Benning, V.M.; Daguanno, J.A. A Review of Multichannel Indexes of Class Separability. *Int. J. Remote Sens.* **1987**, *8*, 331–350. [CrossRef]

42. Qiu, B.W.; Fan, Z.L.; Zhong, M.; Tang, Z.H.; Chen, C.C. A New Approach for Crop Identification with Wavelet Variance and JM Distance. *Environ. Monit. Assess.* **2014**, *186*, 7929–7940. [CrossRef] [PubMed]

43. Kruse, F.A.; Lefkoff, A.B.; Boardman, J.W.; Heidebrecht, K.B.; Shapiro, A.T.; Barloon, P.J.; Goetz, A.F.H. The Spectral Image-Processing System (Sips)—Interactive Visualization and Analysis of Imaging Spectrometer Data. *Remote Sens. Environ.* **1993**, *44*, 145–163. [CrossRef]

44. You, S.X.; Zheng, Q.M.; Lin, Y.; Zhu, C.M.; Li, C.L.; Deng, J.S.; Wang, K. Specific Bamboo Forest Extraction and Long-Term Dynamics as Revealed by Landsat Time Series Stacks and Google Earth Engine. *Remote Sens.* **2020**, *12*, 3095. [CrossRef]

45. Souza, C.M.; Shimbo, J.Z.; Rosa, M.R.; Parente, L.L.; Alencar, A.A.; Rudorff, B.F.T.; Hasenack, H.; Matsumoto, M.; Ferreira, L.G.; Souza, P.W.M.; et al. Reconstructing Three Decades of Land Use and Land Cover Changes in Brazilian Biomes with Landsat Archive and Earth Engine. *Remote Sens.* **2020**, *12*, 2735. [CrossRef]

46. Cutler, A.; Cutler, D.R.; Stevens, J.R. Random Forests. In *Ensemble Machine Learning*; Springer US: Boston, MA, USA, 2012; pp. 157–175.

47. Congalton, R.G.; Green, K. *Assessing the Accuracy of Remotely Sensed Data: Principles and Practices*; CRC Press: Boca Raton, FL, USA, 2019.

48. Sokolova, M.; Japkowicz, N.; Szpakowicz, S. *LNAI 4304—Beyond Accuracy, F-Score and ROC: A Family of Discriminant Measures for Performance Evaluation*; Springer: Berlin/Heidelberg, Germany, 2006.

49. Man, C.D.; Nguyen, T.T.; Bui, H.Q.; Lasko, K.; Nguyen, T.N.T. Improvement of Land-Cover Classification over Frequently Cloud-Covered Areas Using Landsat 8 Time-Series Composites and an Ensemble of Supervised Classifiers. *Int. J. Remote Sens.* **2018**, *39*, 1243–1255. [CrossRef]

50. Foody, G.M. Assessing the Accuracy of Land Cover Change with Imperfect Ground Reference Data. *Remote Sens. Environ.* **2010**, *114*, 2271–2285. [CrossRef]

51. Ji, Q.L.; Liang, W.; Fu, B.J.; Zhang, W.B.; Yan, J.W.; Lu, Y.H.; Yue, C.; Jin, Z.; Lan, Z.Y.; Li, S.Y.; et al. Mapping Land Use/Cover Dynamics of the Yellow River Basin from 1986 to 2018 Supported by Google Earth Engine. *Remote Sens.* **2021**, *13*, 1299. [CrossRef]

52. Qian, D.W.; Cao, G.M.; Du, Y.G.; Li, Q.; Guo, X.W. Impacts of Climate Change and Human Factors on Land Cover Change in Inland Mountain Protected Areas: A Case Study of the Qilian Mountain National Nature Reserve in China. *Environ. Monit. Assess.* **2019**, *191*, 486. [CrossRef]

53. Peng, Q.; Wang, R.H.; Jiang, Y.L.; Li, C. Contributions of Climate Change and Human Activities to Vegetation Dynamics in Qilian Mountain National Park, Northwest China. *Glob. Ecol. Conserv.* **2021**, *32*, e01947. [CrossRef]